

Quantum vs classical thermal model for resistive random access memories

Enrique Moreno Perez^a

^aCzech Technical University in Prague: Prague, CZ, Dept. of Electromagnetic Field, Faculty of Electrical Engineering, CTU Technická N2, Prague, 16627, Prague 6-Dejvice, Czech Republic

SUPERVISOR INFO

Emilio Ruiz Reina
Department of Applied Physics II, University of Málaga, Málaga, Spain

ABSTRACT

The additional computation complexity and the time consumed in quantum thermal transport modeling of a nanometric resistive random access memory cell have proven to be truly rewarded. This is because the semi-classical and classical approaches lead to results considerably far from the quantum ones. In addition, in this work, a methodology for characterization of the properties of the conductive filament has been introduced. For this purpose, simulation results have been combined with measurable data in the cell as well as with properties of the materials used in its construction.

1. Introduction

The human brain consumes, in mean, an approximate power of 80 watts Balasubramanian (2021) and it is by far the most complex biological organ that we know nature has been able to produce. More than one hundred billion nerve cells and many more contact points between them provide our brain with capabilities that no supercomputer can match to this day Society (2018). Paradoxically, the brain's production does not require exotic materials, particularly metals that are not very abundant in the earth's crust. That is, it is built with the dispersion of resources that we find on the planet, which implies an even more significant reduction in the energy necessary to concentrate these scarce materials Alicia Valero (2014). And since no such energy is required to build a brain, it is extremely energy efficient, especially if it is compared with the AI's current syntactical taxonomy. In addition, if we compare a human brain with a high-performance computing facility, at the operation time in terms of energy consumed, its performance is extraordinary. Especially now that we are witnessing the transition of a new era in which we will stop managing energy abundance to start managing scarcity, given that the maximum production peaks of non-renewable resources have either already passed or are close Agency, we should wonder how to maintain the essential digitization of our societies. In that way, power/energy optimization is critical. Additionally, we have many reasons to reduce our energy intake very considerably globally because we are already dealing with the sixth mass extinction of species Ceballos, Ehrlich and Dirzo (2017); Cowie, Bouchet and Fontaine (2022), and climate change is a big threat that is pushing the atmospheric conditions to climate destabilization. This might mean the end of the Holocene climate moderation and the impossibility of predicting the weather, that is, the end of the agriculture and in this way the end of our species too Nations (2022); BORDERA JUAN (2022). In

this context, in which a century of opportunities opens up for engineers since much of the current technology has to be redesigned, metal-insulator-metal memory technologies are presented as an alternative. In particular, we focused this study on resistive-switching memory devices (RRAMs, Resistive Random-Access Memories) which are becoming to replace non-volatile memory or dynamic random-access memory Hui, Liu, Hodge, Carey, Wen, Torrisi, Galhena, Tomarchio, Lin, Moreno, Roldan, Koren, Ferrari and Lanza (2021) as well as their use for artificial intelligence, since they have shown all neuronal synopsis possibilities mimics the original low energy consumption Lin, Guha and Ramanathan (2018).

The resistive change of the RRAMs is based on the formation of one or more conductive filaments (CF), which is the most frequent case, then then device changes between two resistive states that are obtained by the formation and destruction of these filaments. In this type of device, after the filament formation process in a virgin dielectric (Forming state), there is a change from a High Resistance State (HRS) to a Low Resistance State (LRS) D. Maldonado (2022). Afterwards, the device can change back to the HRS by partially dissolving the CF, which would be RESET process and, subsequently, the CF could be regenerated again during the SET process, going back from the HRS to the LRS Aldana, García-Fernández, Romero-Zaliz, Jiménez-Molinos, Gómez-Campos and Roldán (2018); Pérez, Maldonado, Acal, Ruiz-Castro, Alonso, Aguilera, Jiménez-Molinos, Wenger and Roldán (2019). Change HRS to LRS is name a cycle, where variability cycle to cycle is one of the most problems that is studying in RRAM today. There are two main types of devices based on the physical phenomena that underpin the resistive switching operation. If a conductive filament of metal ions from an active electrode is formed, they are called Conductive Bridge RAM (CBRAM) or Electrochemical memories (ECM), if the conductive filament is formed by grouping oxygen vacancies, they are called Valence Change Memories (VCM). We can also classify RRAMs depending on the polarity of the voltage used to produce the resistance change processes: bipolar

 enrique@moreno.ws (E.M. Perez)

 <https://elmag.fel.cvut.cz/oblasti-vyzkumu/cem/> (E.M. Perez)

ORCID(s): 0000-0002-5304-1311 (E.M. Perez)

and unipolar. In unipolar devices based on electrochemical mechanisms, the creation of CF is related to the generation of ions at the active electrode interface and their oxidation in the dielectric until CF is formed. However, the destruction of CF is mainly based on thermal phenomena. The increase in temperature in the RESET process increases the probability of oxidation of the atoms and the rate of diffusion of the ions, leading to the destruction of the filament. It is known that ionic diffusion and drift processes allow changing properties of dielectric/electrode interfaces or forming conductive filaments in the dielectric. These changes modify the resistance of the devices Funck and Menzel (2021) and enable resistive switching. In Funck and Menzel (2021) the authors develop a microscopic picture of the conduction. In coherence with Funck and Menzel (2021) the simulations carried out here suggest a conduction limited by a tunneling through the Schottky barrier at the metal electrode contact. The thermal effects that occur in resistive switching are essential to explain most of the operational characteristics of RRAMs Roldán, González-Cordero, Picos, Miranda, Palumbo, Jiménez-Molinos, Moreno, Maldonado, Baldomá, Moner Al Chawa, de Benito, Stavrinides, Suñé and Chua (2021). That is the reason why a difference in the modeling and simulation process regarding the temperature reached by the filament is crucial. In what follows we will demonstrate how a full quantum approach leads to different results for maximum filament temperature and therefore such an approach is essential in modeling and simulating memristors.

2. Modeling by a multi-physics system of coupled equations

The physical-mathematical modeling of an RRAM cell requires and a multiphysics approach, in which different coupled equations are solved. It is in this context that we use the commercial simulation tool COMSOL. But before entering the subject and beginning to discuss the fundamental elements, the roles they play and the mathematical way of relating and describing them, it is necessary to introduce the form of the computational domain in which all the models will be taken into consideration. To this end, Fig.1 is presented, which through the revolution of a plane allows the generation of a RRAM cell of a cylindrical geometry. The filament in this cell is shaped like a truncated cone. Assuming that the transverse dimension is spatially much larger than the longitudinal one, which coincides with the axis of symmetry of the cylinder, we will have absolute independence of the shape of the cell. Since if the cell were square or even triangular, the effects would be equally defined in a local region close to the filament. So we have two important issues to consider. First of all we will carry out a simulation in two dimensions. This is what COMSOL calls a 2D-axisymmetric domain, which will allow us to generate 3D solutions with a reduced number of finite elements. At the same time, we will truncate that domain with an artificial boundary condition to extend the transverse direction of the RRAM cell. Artificial truncation of the domain can be handled in

several ways. Here we employ which COMSOL calls an Infinite Element Domain node which applies a real-valued coordinate scaling to a layer of virtual domains surrounding the physical region of interest. When the dependent variables vary slowly with radial distance from the center of the physical domain, the finite elements can be stretched in the radial direction such that boundary conditions on the outside of the infinite element layer are effectively applied at a very large distance from any region of interest, just a re-scaling of the metric which results in an extension of the domain. We then consider a two-dimensional domain that has been

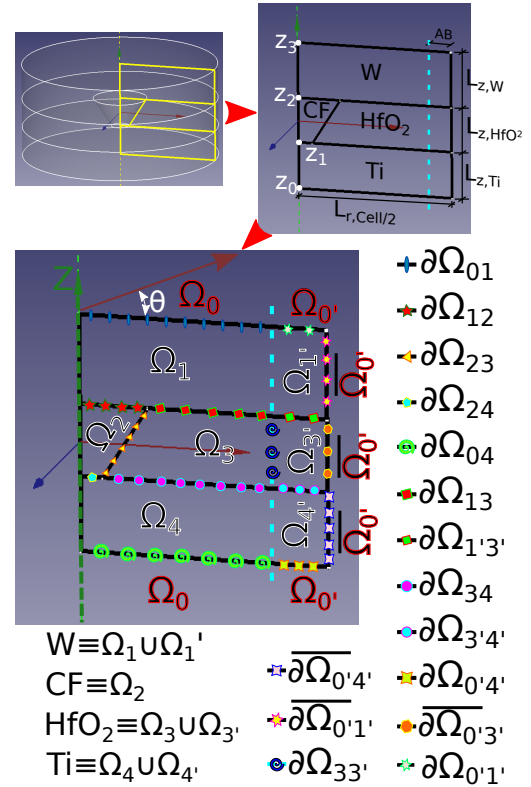


Figure 1: This figure relates the material components with the labels that allow their identification quickly and unambiguously. It also shows the labels that identify the boundaries between materials or domains, whether real or artificial.

divided into regions. Each of the regions corresponds to a material component of the cell. That is, in the longitudinal section of the cell, Fig.1 illustrates the materials that have been labeled as follows. $\Omega_1 \cup \Omega_{1'}$ and $\Omega_4 \cup \Omega_{4'}$ are the metallic contacts. $\Omega_3 \cup \Omega_{3'}$ is the oxide that isolates both contacts. Ω_2 is the filament that percolates the insulator and connects the aforementioned metallic contacts. Naturally, we use only two (r, z) of the three Cylindrical coordinates (r, θ, z) for a proper description. In these coordinates, arrived at a certain radial position, we carry out a truncation of the computational domain, which would extend far beyond that position. Fig.1 shows this truncation with a cyan vertical dash line. The artificial region is the one constituted by the union of domains $\Omega_1 \cup \Omega_{3'} \cup \Omega_{3'}$. We will call each of these regions depicted in Fig.1 as subdomains. So the $\Omega_1 \cup \Omega_{1'}$,

subdomain is tungsten, the $\Omega_4 \cup \Omega_4'$ subdomain is titanium, the $\Omega_3 \cup \Omega_3'$ subdomain is oxide of hafnium, and the Ω_2 subdomain is the conducting filament. We utilize the labels of the subdomains to define the borders between them in such a way that the border between the subdomain Ω_1 and Ω_3 is designated as $\partial\Omega_{13}$. This boundary $\partial\Omega_{13}$ would be separating tungsten from hafnium oxide in the non-artificial domain region. When the border is located within the artificial domain we use the same nomenclature, so the border that separates the $\Omega_{1'}$ subdomain from the $\Omega_{3'}$ subdomain within the artificial region would be $\partial\Omega_{1'3'}$. To completing this assignment of labels, it is necessary to mention that the zero subdomain Ω_0 has been used to identify any region that is outside the computational domain. In this naming strategy, when a Ω_0 subdomain is in the artificial region a tilde has been added, being $\Omega_{0'}$. Finally, mention that when this zero subdomain is next to a vertical border, in the artificial region, a bar has been added on the mentioned subdomain, being in this case $\overline{\Omega_{0'}}$.

The fundamental magnitude from which a transition from a conducting state to an open-circuit state occurs is related to temperature. But in the determination of this temperature through the resolution of the heat equation in a steady-state, we need to determine which is the heat source. Here we assume its nature is related to the Joule effect and in this way, to the electric current that circulates through the cell as well as the electric field that polarized it.

2.1. Electric current and field

In this context the current flowing through the cell has to be determined. Since the thickness of the insulator, hafnium of oxide, is in the range of a few nanometers, we understand that a quantum approach is necessary. We must therefore consider the tunnel effect current that is added to the conductive or drive current that would circulate through the cell conducting filament. In the set of equations that follows, those essential quantities are determined to prescribe the heat source.

$$\nabla \cdot \vec{J}_e(\vec{r}) = \sum_j Q_{j,v}(\vec{r}) \quad (1)$$

$$\vec{J}_e(\vec{r}) = \sigma(\vec{r})\vec{E}(\vec{r}) \quad (2)$$

$$\vec{E}(\vec{r}) = -\nabla V(\vec{r}) \quad (3)$$

$$\hat{n} \cdot (\vec{J}_1(\vec{r}_s) - \vec{J}_2(\vec{r}_s)) = \sum_j Q_{j,s}(\vec{r}_s) \quad (4)$$

Where $\vec{J}_e(\vec{r})$ is the density of electric current, $\sum_j Q_{j,v}$ is the sum of current volumetric sources/sinks, $\sigma(\vec{r})$ is the electric conductivity, $\vec{E}(\vec{r})$ is the electric field, $V(\vec{r})$ is the electric potential, \hat{n} is a unit vector at the interface where a $\vec{J}_1(\vec{r}_s) - \vec{J}_2(\vec{r}_s)$ current density balance is injected and $\sum_j Q_{j,s}(\vec{r}_s)$ is the sum of current surface sources/sinks on a given interface. In brief, the dependent variable of the system of equations is the voltage, and therefore we are solving Laplace equation with no current volumetric sources/sinks

contribution $\forall j Q_{j,v} = 0 \left[\frac{A}{m^3} \right]$. The electric field and the current derive from it, since it is from this electric potential that they are calculated. On the other hand, the equation (4) allows us to introduce the quantum tunneling current into the coupled system of equations. We do this by a surface current density $Q_{j,s}(\vec{r}_s) = \hat{n} \cdot (\vec{J}_1(\vec{r}_s) - \vec{J}_2(\vec{r}_s)) = J_{1,z}(\vec{r}_s) - J_{2,z}(\vec{r}_s) \equiv J_{QM} \left(V_{QM}(\vec{r}_s), \frac{1}{G(\vec{r}_s)} \right)$ placed in one of the insulator faces $\vec{r}_s \in \partial\Omega_{34}$. A little later we will see how this quantum tunneling current is determined. Before introducing the boundary conditions that we apply to this set of equations, it is important to mention that this is where we find the core of this contribution. the object of this work is none other than the determination of the properties of the conducting filament of the RRAM cell. These properties essentially refer to its ability to conduct electricity. The electrical conductivity mathematical model of the conducting filament is governed parametrically by two parameters, the filament conductivity σ_{CF} and resistivity temperature coefficient α_T . In the following expression, we find the mathematical model that prescribes the electrical conductivity of all the materials/subdomains consider in the RRAM cell.

$$\sigma(\vec{r}) = \begin{cases} \sigma_W(T(\vec{r})) & \text{if } \vec{r} \in \Omega_1 \cup \Omega_1' \\ \frac{\sigma_{CF}}{1+\alpha_T(T(\vec{r})-T_0)} & \text{if } \vec{r} \in \Omega_2 \\ \sigma_{HfO_2}(T(\vec{r})) & \text{if } \vec{r} \in \Omega_3 \cup \Omega_3' \\ \sigma_{Ti}(T(\vec{r})) & \text{if } \vec{r} \in \Omega_4 \cup \Omega_4' \end{cases} \quad (5)$$

Where $\sigma_W(\vec{r})$, $\sigma_{HfO_2}(\vec{r})$ and σ_{Ti} are the electric conductivity of tungsten, oxide of hafnium and titanium respectively. For the metals and the dielectric insulator we use experimental data which are represented in Fig.2. The electrical

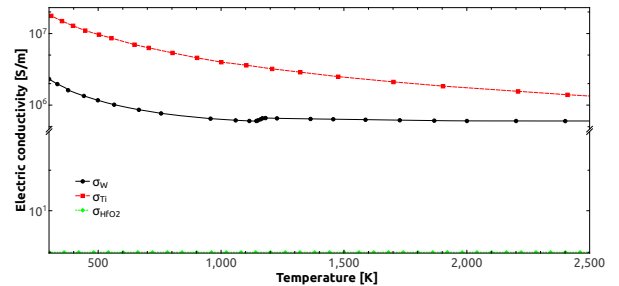


Figure 2: The figure represents the electrical conductivities of some of the materials used in the RRAM cell versus the temperature.

conductivity of tungsten plotted versus the temperature in Fig.2, has been taken from the bibliographical source Desai, Chu, James and Ho (1984). In the same way, the electrical conductivity of titanium has been taken from the bibliographical source Dyos and Farrell (2012). Finally, in the case of hafnium oxide, the electrical conductivity has been taken from the bibliographical source Callegari, Cartier, Gribelyuk, Okorn-Schmidt and Zabel (2001).

2.1.1. Boundary condition Dirichlet

We can consider that in the solution of Poisson equation the electric potential is prescribed as a Dirichlet-type boundary condition of two types. One type would be imposed on contours, which would impose the polarization of the RRAM cell.

$$V(\vec{r}) = \begin{cases} 0V & \text{if } \vec{r} \in \partial\Omega_{01} \cup \partial\Omega_{0'1'} \\ 1V & \text{if } \vec{r} \in \partial\Omega_{04} \cup \partial\Omega_{0'4'} \end{cases} \quad (6)$$

On the other hand, there is a correction to the potential due to the solution of the Schrodinger-Poisson equation, which leads to the Dirichlet boundary condition $V(\vec{r}) = V_{QM}(\vec{r})$ applied on $\forall \vec{r} \in \Omega_3$. This coupled solution of the Poisson equation together with the Schrodinger equation slightly modifies the potential and is essential to know the real distribution of the potential in the insulator. This is important since the quantum tunneling current depends on this electrical potential.

2.1.2. Boundary condition Neumann

To give consistency to the solution of the system of equations we have to impose a current flow on the outer borders of the RRAM cell, that is, on the side walls. Thus we impose the following Neumann-type boundary condition on the outer walls.

$$\frac{\partial V(\vec{r})}{\partial \hat{n}} \Rightarrow \vec{J}(\vec{r}) \cdot \hat{n} = 0 \text{ if } \vec{r} \in \overline{\partial\Omega_{0'1'}} \cup \overline{\partial\Omega_{0'3'}} \cup \overline{\partial\Omega_{0'4'}} \quad (7)$$

Hence we have the electric field and the electric current density both derived from the electric potential that we have just calculated. This allows us to model the heat sources and deal with the heat equation. Moreover, the current equations are coupled with the heat equation since the material properties in the studied equations depend on temperature.

2.2. Heat equation

In this section we will start from the stationary filament hypothesis. This means that although there is an internal dynamic of ions in the filament, when it has been formed, the process of variation or transport is extremely slow. Which means that the convective current that could exist in the filament can be neglected. Thus, the equation $\rho(T(\vec{r})) C_P(T(\vec{r})) \vec{u}(\vec{r}) \cdot \nabla T(\vec{r}) + \nabla \cdot \vec{q}(\vec{r}) = Q_h(\vec{r})$ becomes a canonical Poisson equation for the temperature since the present transport speed is assumed to be zero $\vec{u}(\vec{r}) \simeq \vec{0}$. This leads to the following system of equations to calculate the temperature.

$$\nabla \cdot \vec{q}(\vec{r}) = Q_h(\vec{r}) \quad (8)$$

$$\vec{q}(\vec{r}) = -k(\vec{r}) \cdot \nabla T(\vec{r}) \quad (9)$$

$$Q_h(\vec{r}) = \vec{J}_e(\vec{r}) \cdot \vec{E}(\vec{r}) \quad (10)$$

Where $\vec{q}(\vec{r})$ is the heat flux (also called Fourier current), Q_h is the volumetric power source/sink, $k(\vec{r})$ is the tensor of thermal conductivity, and $T(\vec{r})$ is the temperature. From the previously made calculations we can derive the shape of the volumetric power source $Q_h(\vec{r})$, from the electric

potential and the electric conductivity. if we consider that $\nabla V(\vec{r}) \cdot \nabla V(\vec{r}) = \|\nabla V(\vec{r})\|^2$ we arrive at the expression:

$$Q_h(\vec{r}) = \begin{cases} \sigma_W(\vec{r}) \|\nabla V(\vec{r})\|^2 & \text{if } \vec{r} \in \Omega_1 \cup \Omega'_1 \\ \frac{\sigma_{CF} \|\nabla V(\vec{r})\|^2}{1 + \alpha_T(T(\vec{r}) - T_0)} & \text{if } \vec{r} \in \Omega_2 \\ \sigma_{HfO_2}(\vec{r}) \|\nabla V(\vec{r})\|^2 & \text{if } \vec{r} \in \Omega_3 \cup \Omega'_3 \\ \sigma_{Ti}(\vec{r}) \|\nabla V(\vec{r})\|^2 & \text{if } \vec{r} \in \Omega_4 \cup \Omega'_4 \end{cases} \quad (11)$$

Similarly we have to apply boundary conditions to the heat equation to solve it in the computational domain.

2.2.1. Boundary condition Dirichlet

The Dirichlet-type boundary condition on temperature is quite simple to implement since it consists of imposing a known temperature T_0 on the external faces of the metallizations.

$$T(\vec{r}) = \begin{cases} T_0 & \text{if } \vec{r} \in \partial\Omega_{01} \cup \partial\Omega_{0'1'} \\ T_0 & \text{if } \vec{r} \in \partial\Omega_{04} \cup \partial\Omega_{0'4'} \end{cases} \quad (12)$$

2.2.2. Boundary condition Neumann

For the case of the boundary condition on heat flux we need to do a little trick that aims to extend the artificial truncation already discussed previously. The idea is to maintain the flow of heat that reaches a wall, making it continue to have the same value in that wall.

$$\frac{\partial T(\vec{r})}{\partial \hat{n}} \Rightarrow -\vec{q}(\vec{r}) \cdot \hat{n} = q_0 \text{ if } \vec{r} \in \overline{\partial\Omega_{0'1'}} \cup \overline{\partial\Omega_{0'3'}} \cup \overline{\partial\Omega_{0'4'}} \quad (13)$$

This is done by setting a power flow per unit area q_0 . Where

$$q_0 = \hat{r} \cdot \begin{pmatrix} k_{rr} & k_{r\theta} & k_{rz} \\ k_{\theta r} & k_{\theta\theta} & k_{\theta z} \\ k_{zr} & k_{z\theta} & k_{zz} \end{pmatrix} \nabla T(\vec{r}) = k_{rr} \nabla_r T(\vec{r}).$$

Rigorously speaking, we would have $(k_{rr} + k_{\theta r} + k_{zr}) \nabla_r T$, but since it is a symmetric diagonal tensor, things are simplified, leaving the expression seen above.

2.3. Self-consistent model for tunneling current

In the self-consistent modeling for tunneling current we consider a diagram of energy bands corresponding to the multilayer that forms the RRAM cell. In the diagram portrayed in Fig.3 we see that there are two tunneling current densities whose difference gives us the total quantum tunneling current density. The objective of this section will be to model these currents. In this modeling process the determination of the potential barrier is the first step. In Fig.3 we assume a single Fermín level since it is a system in stationary equilibrium. In this case we have got two different work functions and a single electrical affinity corresponding to the insulator, the hafnium oxide. The insulating film is assumed to be sufficiently thin (in the nano-meter scale), charge trapping may be ignored Rose (1955); Frank and Simmons (1967); Zhang (2015). The electrons in the electrodes would see a potential barrier formed between the two electrodes given by the expression:

$$\Phi(r, z) = E_F + W f_W - \chi_{HfO_2} + \frac{(W f_{Ti} - W f_W) z}{D(r, z)}$$

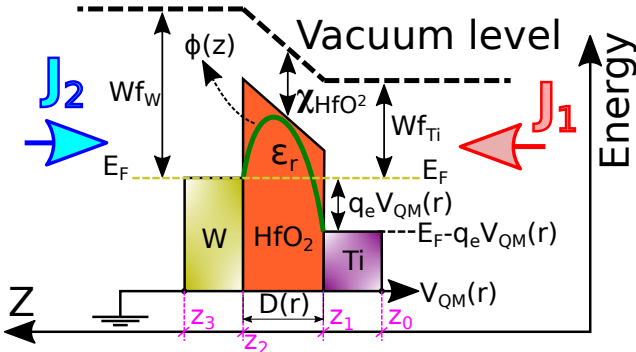


Figure 3: Energy band diagram of the considered RRAM cell, a dissimilar metal-insulator-metal tunneling junction.

$$+ \Phi_{image}(r, z) + q_e V_{QM}(r, z) + Y_{zc}(r, z) \quad (14)$$

Where E_F is the Fermi level, Wf_W is the work function of the tungsten, χ_{HfO_2} is electron affinity of the insulator, $\Phi_{image}(r, z)$ is the image charge potential energy defined in appendix A, $Y_{zc}(r, z)$ is electron exchange-correlation potential also defined in appendix A, q_e is the electron charge and $V_{QM}(r, z)$ is the Poisson-Shrödinger electric potential which crosses the quantum barrier.

It is clear that although Fig.3 only shows one spatial dimension (Z-axis), the direction perpendicular to the dielectric sandwich, we will have to assume that along the entire plane of the RRAM cell there is a variation of the quantum tunneling current. Given the symmetry of revolution we can reduce the dependency to just two variables. The radial direction and the direction perpendicular to the potential barrier, that is, the Z axis.

The probability $\varphi(E', r)$ that an electron with longitudinal energy E' , normal to the surface, can penetrate the potential barrier of height $\Phi(r, z)$ is given by the Wentzel-Kramers-Brillouin-Jeffreys approximation Bates (2013); Zhang (2015); Banerjee and Zhang (2019),

$$\varphi(E', r) = e^{-\frac{2}{\hbar} \int_{z_1}^{z_2} \sqrt{2m(\Phi(r, z) - E')} dz} \quad (15)$$

Where z_1 and z_2 are the two roots of $\Phi(r, z) - E' = 0$.

By means of $N_1(E', r, z_1)dE'$, $N_2(E', r, z_2)dE'$ and the probability $\varphi(E', r)$ we determine the current density tunneling through the barrier from electrode 1, $J_{1,z}(r, z_1)$ and the current density tunneling through the barrier from electrode 2, $J_{2,z}(r, z_2)$. Their expression are as follows:

$$J_{1,z}(r, z_1) = q_e \int_{-\infty}^{\infty} N_1(E', r, z_1) \varphi(E', r) dE' \quad (16)$$

$$J_{2,z}(r, z_2) = q_e \int_{-\infty}^{\infty} N_2(E', r, z_2) \varphi(E', r) dE' \quad (17)$$

Where $N_1(E', r, z_1)dE'$ is the total number of electrons inside the tungsten electrode with longitudinal energy between E' and $E' + dE'$ impinging on the surface of the tungsten electrode across a unit area per unit time, and $N_2(E', r, z_2)dE'$ is the total number of electrons inside the titanium electrode with longitudinal energy between E' and $E' + dE'$ impinging on the surface of the titanium electrode

across a unit area per unit time, both calculated by free-electron theory of metal Altmann (2013). These magnitudes can be calculated using the bellow equations:

$$N_1(E', r, z_1) dE' = \Theta_1(r, z_1) \ln \left(1 + e^{-\frac{E' + q_e V_{QM}(r, z_1) - E_F}{k_B T(r, z_1)}} \right) \quad (18)$$

$$N_2(E', r, z_2) dE' = \Theta_2(r, z_2) \ln \left(1 + e^{-\frac{E' - E_F}{k_B T(r, z_2)}} \right) \quad (19)$$

Where $\Theta_1(r, z_1) = \frac{mk_B T(r, z_1)}{2\pi^2 \hbar^3}$ and $\Theta_2(r, z_2) = \frac{mk_B T(r, z_2)}{2\pi^2 \hbar^3}$ are the number of electrons at temperature $T(r, z_1)$ and $T(r, z_2)$ respectively, k_B is the Boltzmann constant, m is the electron mass and \hbar is the Planck reduced constant.

As can be seen in these expressions as well as the ones that appear in appendices A and B, there is a magnitude that is essential for the determination of the quantum tunneling current. It is the electrical potential $V_{QM}(r, z)$ that is distributed inside the dielectric insulator. Next subsection is dedicated to the determination of the potential electric by solving the coupled Poisson-Shrödinger equation.

2.4. Poisson-Shrödinger equation

Inside the oxide of hafnium (region Ω_3) we employ the mean-field theory Frank and Simmons (1967); Lau, Chernin, Colombant and Ho (1991); Ang, Kwan and Lau (2003); Lin Wu and Li (2012); Zhang (2015); Banerjee and Zhang (2019) to solve the electric potential $V_{QM}(\vec{r})$. Therefore, we solve the coupled Shrodinger equation and the Poisson equation,

$$\nabla \cdot \vec{D}(\vec{r}) = \rho_v(\vec{r}) \quad (20)$$

$$\vec{D}(\vec{r}) = \epsilon_r \epsilon_0 \vec{E}_{QM}(\vec{r}) \quad (21)$$

$$\vec{E}_{QM}(\vec{r}) = -\nabla V_{QM}(\vec{r}) \quad (22)$$

$$H\psi(\vec{r}) = E\psi(\vec{r}) \quad \vec{r} \in \Omega_3 \quad (23)$$

$$n_\rho(\vec{r}) = \sum_m \sum_i \frac{2g_{i,m} |\Psi_{i,m}(\vec{r})|^2}{1 + e^{\frac{E_{i,m} - E_F}{k_B T}}} \quad (24)$$

$$\rho_v(\vec{r}) = q_e n_\rho(\vec{r}) e^{-\alpha - \frac{q_e(V_{QM}(\vec{r}) - V_{QM,old}(\vec{r}))}{k_B T(\vec{r})}} \quad (25)$$

Where $\vec{D}(\vec{r})$ is the electric displacement vector, ϵ_r is the insulator electric permittivity, H is the Hamiltonian operator, $\psi(\vec{r})$ is the Shrödinger's wave equation, g_i is the valley degeneracy factor, $E_{i,m}$ is the a set of eigenenergies $i - th$ which corresponds to a set of normalized wave functions $\Psi_{i,m}(\vec{r})$, both produced by the Schrödinger equation solution. So in this approach the Hamiltonian operator H is a function of $V_{QM}(\vec{r})$ (see section B). More over, in the Schrödinger equation the potential energy term is $V_e(\vec{r}) = q_e V_{QM}(\vec{r})$. In appendix B $V_e(\vec{r})$ is expressed as the element $V_{e,mm}$. So as to determine the density of electrons $n_\rho(\vec{r})$, there should be a summation over several indexes. For instance, we can consider the azimuthal quantum number and the eigenenergy levels (for each azimuthal quantum number). However, for simplicity in solving this system of coupled

partial differential equations we have considered a single azimuthal quantum number ($m=0$). This issue should not be closed without commenting that the α parameter that appears in the above equations is a tuning trick used by COMSOL developers to speed up the method numerical convergence. Let us now consider the boundary conditions necessary to solve the system of equations.

2.4.1. Boundary condition Dirichlet

In the first place we have to consider Dirichlet-type boundary conditions that are applied to the electric potential. In this case, we fix or imposed the electric potential on the perimeter of the insulator by means of the external potential calculated in the entire RRAM cell. The modification over the global electrical potential that the quantum potential has in the region, the insulator, is applied by means of a correction in the global electric potential across of the entire RRAM cell.

$$V_{QM}(\vec{r}) = V(\vec{r}) \text{ if } \vec{r} \in \partial\Omega_{13} \cup \partial\Omega_{23} \cup \partial\Omega_{34} \quad (26)$$

2.4.2. Boundary condition Neumann

Regarding the Neumann-type boundary conditions, we specify three conditions. One on the electric potential, through the electric displacement vector, which must remain constant at the interface $\partial\Omega_{3'}$, and is the following condition, and two boundary conditions on the Shrodinger wave equation.

$$\hat{n} \cdot \vec{D}(\vec{r}) = \hat{n} \cdot \vec{D}_0(\vec{r}) \text{ if } \vec{r} \in \partial\Omega_{3'} \quad (27)$$

On some boundaries we applied zero flux boundary condition. It imposed that the normal component of the probability current density is set to zero by the nature of the equation system.

$$\hat{n} \cdot \nabla\psi(\vec{r}) = 0 \text{ if } \vec{r} \in \partial\Omega_{34} \cup \partial\Omega_{23} \cup \partial\Omega_{13}$$

Finally, to express that the media Ω_3 continues into the domain $\Omega_{3'}$ we apply a open boundary condition which allows outgoing waves leave the modeling domain Ω_3 without being reflected back from the external boundaries that enclose $\Omega_{3'}$.

$$\hat{n} \cdot \nabla\psi(\vec{r}) = j \left(\frac{1}{\hbar} \sqrt{\frac{2(E-V)}{\hat{n} \cdot m_{ef}^{-1} \cdot \hat{n}}} \right) \psi(\vec{r}) \text{ if } \vec{r} \in \partial\Omega_{3'}$$

In what follows we describe the numerical methodology necessary to implement the algorithms that solve the physics described so far.

3. Some implementation issues

The quantum current density is entered into COMSOL using an MATLAB function. This function calculates the density of quantum tunneling current $\vec{J}_{QM}(r, z)$ which is introduced into the model through the COMSOL boundary condition called Boundary Current Source. Fig.4a) and Fig.4b) sketch the coupling. This function uses four variables to enter the local insulator thickness, given by the reciprocal distance (see appendix A.1), the local voltage that biases

the oxide, and the two temperatures at both metal-insulator interfaces. The procedure begins by solving a first study, in a classical way¹. From that classic solution we carry out a second study in which the COMSOL physical module, introduced in 2.1, is consider assuming a quantum tunneling current coherent with the global potential. That is, from the initial potential distribution throughout the entire RRAM cell, where $V_{QM}(r, z) = V(r, z)$ in the region Ω_3 . Finally, by utilizing this semi-classical approach solution as the initial state of the full quantum approach, that computes the model 2.4 (to determine $V_{QM}(r, z)$) in a third study, we determine accurately the main dependent variable, temperature and voltage in the entire cell. Therefore, the third study repeats in a loop a steady-study followed by the Pissou-Shrodinger-study until COMSOL-solvers find convergence.

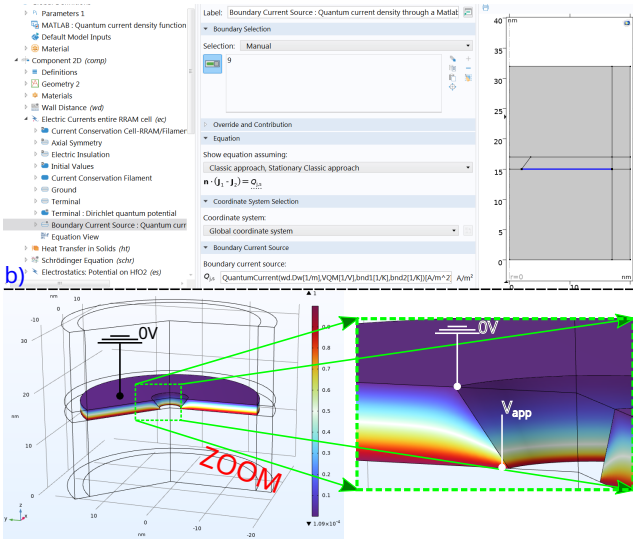
At this point some details about the MATLAB function are necessary. The tunneling current density relies upon four parameters, the bias voltage $V_{app}(\vec{r}) = V_{QM}(r, z_1) - V_{QM}(r, z_2)$, the insulator thickness $D(\vec{r})$, and the adjacent temperatures $T_1(r, z_1)$ and $T_2(r, z_2)$ (\vec{r}) to the insulator-metal faces. However, we depart from a two coordinate map, (r, z) which produces some repeated values of the quaternary set (V_{app}, D, T_1, T_2) , so we have a surjective application. This considerably reduces the computation time since there are redundant data, something that can be avoided if the MATLAB algorithm/function is used to obtain a cloud of numerical data that can be entered in COMSOL through a multivariable interpolation function that provides the same results. This means considerably less time in the calculations, although it does not have the same degree of precision.

The reason why we have to choose a distance set $D(\vec{r})$ has to do with the filament being considered as a part of the metal contacts. That is, there are free electrons that are in the filament that can pass the potential barrier and connect both metals. To obtain the map of coordinates (r, z) that correspond to the distances $D(\vec{r})$, we solve the Eikonal equation that is explained in the appendices A.1. In Fig.5a) we can see how in the region corresponding to the oxide we have determined the reciprocal distance and from this the real distance between the upper wall, which as seen is formed by the tungsten plus the filament, and the lower wall corresponding to the titanium. In turn, the translation of the quantum current density in the map of electrical voltages, distances, and hot metal-insulator interface is shown in Fig.5b), which in turn produces a quantum tunnel current density in the form depicted in Fig.5c).

The results part of this work yields, as we will see in the next section, significant differences in the currents and, above all, in the temperatures between a purely quantum approach and a semi-classical approach. In the characterization procedure we must obtain a set of solutions for a map of parameters

¹In the classical solution there is no tunneling current which leads to $\vec{J}_{QM} = \vec{0}$ and furthermore there is no distribution of charge carriers/electrons in the insulator that modifies the potential in this computational domain region so that we do not have considered the physics presented in the subsections 2.3 and 2.4.

RRAM characterization



$$T_{zc}(r, z) \ll q_e V_{QM}(r, z) + \Phi_{image}(r, z) \Rightarrow \text{new map } (r, z) \rightarrow r$$

$$T_1 \rightarrow \vec{J}_{QM}(r) \Rightarrow \vec{J}_{QM}(V_{QM}, D, T_1, T_2)$$

$$r_2 \rightarrow \vec{J}_{QM}(r)$$

a) **Surjective!** z_1 and z_2 from $\Phi(r, z) - E' = 0 \Rightarrow$
 $D = z_2 - z_1$ and $V_{app} = V_{QM}(z_1) - V_{QM}(z_2)$

Figure 4: a) New map of electric potentials and distances consistent with the coordinate that comes from the COMSOL model. b) COMSOL graphical interface in which the quantum tunneling current density is entered via a current boundary condition at the Ω_{34} interface.

α_T and σ_{CF} . In other words, for each of the combinations of these parameters we have to solve all the physics (all coupled equations) described so far. Based on this challenge we write the following subsection, where we justify why we reduce the computational domain from three dimensions to only two.

3.1. A reduction in the problem size leads to an extremely accurately solution

In Fig.6 we can see how a three-dimensional computational domain, despite being reduced by its symmetries to a quarter of its size, still has many more finite elements than a two-dimensional one. Furthermore, in the two-dimensional domain we can use an extradense mesh and even subgrids in the region of interest as seen in Fig.6. This allows us to solve in seconds a problem that would otherwise require tens of minutes and even hours. Thus, to carry out a mapping of the parameters of interest, α_T and σ_{CF} , to establish which of them, simultaneously, verify the measurable and expected physical conditions. Here what we understand by measurable magnitudes corresponds to the current density that passes through the cell and what is measurable in a laboratory. On the other hand, observing the nanoscale nature of the filament, we can establish at what temperature a fusion of the filament would take place and from this expected behavior, combined with the measurable data of the electronic current density, determine the desired parameters that characterize the RRAM cell. We discuss this in more detail in the results section.

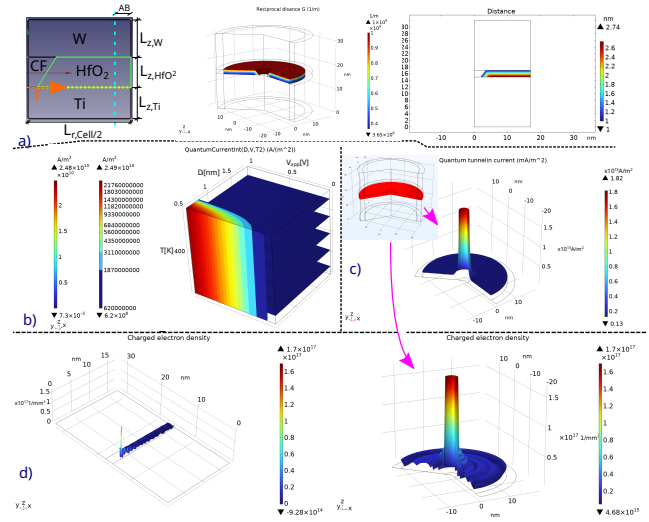


Figure 5: a) Reciprocal distance and real distance in the region of the insulator. b) Quantum Tunneling Current Density as a Function of Voltages, Insulator Thickness and the temperature of the hot metal-insulator interface. c) Distribution of quantum tunneling current density in the region of the RRAM cell where tunneling takes place. d) Distribution of the volumetric density of electrons in the oxide.

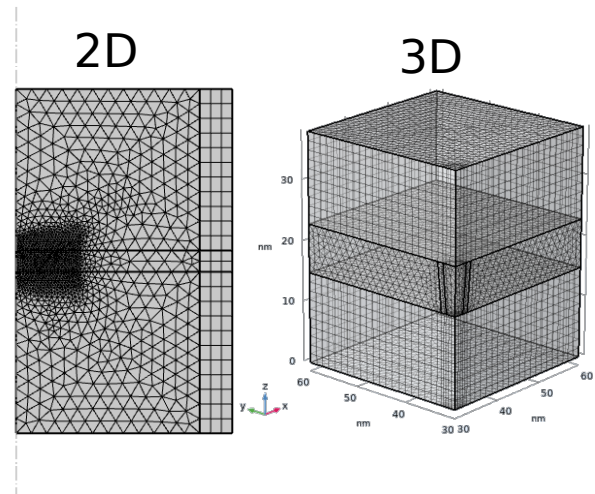


Figure 6: This figure compares the meshing of two computational domains. One two-dimensional and the other three-dimensional for the same physical object.

Another reasonable procedure is the minimum one, that is, above a certain temperature value we assume that fusion always takes place, then in the map (α_T, σ_{CF}) we take the minimum temperature value that has a point in common (the same pair of coordinates (α_T, σ_{CF})) with the measured current density curve and in this way we determine the properties of the filament.

4. Results

We divide this section into two parts. In the first one we show that there are significant differences regarding the

temperature of the filament under a semi-classical modeling approach and another quantum approach. In the second part, a characterization of the filament parameters (α_T, σ_{CF}) is made from experimental data and simulation data using a full quantum approach.

While the electrical conductivity has been considered as a scalar, the thermal conductivity is assumed as a rank two tensor magnitude. In equation (9) there is a dot product between the thermal conductivity and the temperature gradient. This is a COMSOL notation which can be consulted in its Physics Builder Manual. This notation means that we generalize the thermal conductivity to a tensor which allows us to deal with an anisotropic media. If a rank two tensor k is thought of as a matrix \bar{k} (in certain standard basis), $k \cdot \vec{q}$, for \vec{q} a (column) vector, is simply $\bar{k}\vec{q}$. However, $\vec{q} \cdot k$ is $\vec{q}^T \bar{k}$ with t denoting transpose. By using index notation, if $k = k_{ij} \hat{e}_i \hat{e}_j$ and $\vec{q} = q_k \hat{e}_k$, then $k \cdot \vec{q} = q_k k_{ij} \hat{e}_i (\hat{e}_j \cdot \hat{e}_k) = q_k k_{ij} \delta_{jk} \hat{e}_i = k_{ij} q_j$. Fig.7 plots an isotropic thermal conductivity of the media versus the temperature. Nevertheless, assuming in the

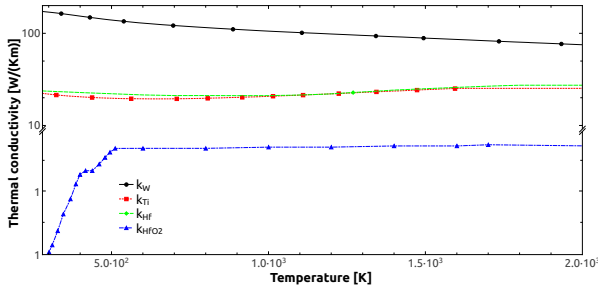


Figure 7: Thermal conductivities of materials versus temperature.

best of cases that the manufacture of the insulator has been carried out by atomic layers deposition, we could prescribe a better thermal conduction in the plane- $r\theta$ than the filament growing direction (z -axis). Thus, we assign 99% of the thermal conductivity of hafnium in the transverse plane to filament growth, while only 90% of this thermal conductivity is assumed in the direction of filament growth.

In Fig.8a) we can see the potential in a longitudinal section that passes through the middle of the filament. Likewise, in Fig.8b) we can see the temperature field in the same longitudinal section. The differences in terms of temperatures are considerable and although the spatial distributions are similar in both cases, in the classical case much higher temperatures are reached than in the quantum case, exceeding 1000 degrees while in the quantum case they do not reach the 800. This is so under the same problem conditions and assuming the same properties of the conducting filament. This was to be expected given that we are considering nano-sized devices and we do not expect high accuracy from a classical descriptor. This result deserves to be analyzed in depth. We understand that the reason why, under the same state of electrical polarization or applied potential, we obtain a smaller source of heat is because part of the current passes, assisted by traps, through the potential or insulating barrier, so that the current flow on the area of the filament is reduced,

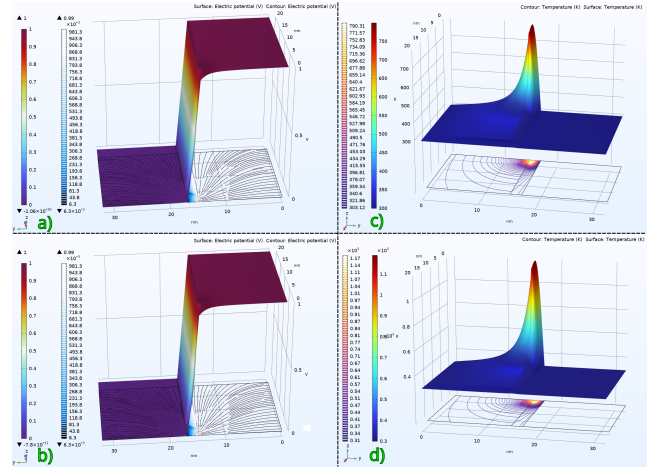


Figure 8: a) Electric potential across the RRAM cell (full-quantum approach). b) Electric potential across the RRAM cell (semi-classical approach). c) Temperature field across the RRAM cell (full-quantum approach). d) Temperature field across the RRAM cell (semi-classical approach).

thus reducing the energy delivered in this region. This is consistent with the literature that actually assumes that the filament itself is a high-density concatenation of traps that facilitates quantum tunneling Funk and Menzel (2021).

We understand the process of characterizing a RRAM cell as the search for a set of parameters that are consistent with measurable magnitudes or deducible from experimental measurements. In this work we hypothesize that we have measured a current density of $1.21 \cdot 10^{11} \frac{A}{m^2}$ and at the same time we have determined a filament melting temperature of 956K. With this information we adjust the parameters that, considering all the properties of the materials and the operating conditions of this RRAM cell, best approximate these experimental data. There are different optimization techniques that allow this search to be carried out and there is also the possibility of performing a parametric scan to interpolate these values. This is exactly what has been done in Fig.9, where fixing both variables, electric current density and filament melting temperature, we have represented the two parameters to be characterized. The magnitudes σ_{CF}

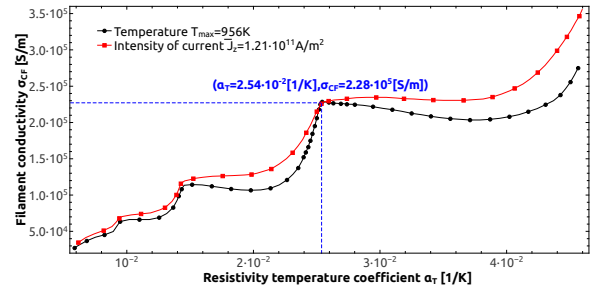


Figure 9: The red line with squares shows the value of the electrical conductivity of the filament versus the resistive temperature coefficient for a given current density. The black curve with circles illustrates the same parameters relationship for a given temperature.

and α_T are discrete variables that have been taken to the continuum by means of interpolation. These interpolation functions have a secant, which is the solution to the problem. Since at such a point both conditions, on the electric current density and the filament melting temperature, are verified. This intersection point of both graphs is represented in blue as the solution of the problem, and its value appears in Fig.9.

A. Image charge potential energy and electron exchange-correlation potential

The image-charge potential energy plays a key role in field emission by lowering the potential barrier, thereby leading to an increase in current density by orders of magnitude Biswas and Ramachandran (2017). Here, the image charge potential energy including the effect of anode screening has been taken from Il'chenko and Goraychuk (2001) (it was used in Lin Wu and Li (2012); Zhang (2015); Banerjee and Zhang (2019)), and its expression so as to determine it is given by the bellow equation,

$$\Phi_{image}(r, z) = \frac{-q_e^2}{8\pi\epsilon_r\epsilon_0} \left(\frac{1}{2z} + \sum_{n=1}^{\infty} \left(\frac{nD(r)}{n^2D^2(r) - z^2} \right) - \frac{1}{nD(r)} \right)$$

Where q_e is the electron charge, $\epsilon_r\epsilon_0$ is the insulator electric permittivity and the D is the dielectric thickness. In our case the thickness of the dielectric depends on the radial position. This is defined as the inverse of the reciprocal distance $D(r) = 1/G(r, z_1)$, a calculation that is explain in detail in appendix A.1.

To avoid quantum tunneling current leaks, it is recommended to use insulators with high electrical permittivity since this increases the image charge potential energy. The electron exchange-correlation potential $Y_{zc}(z)$ is defined also in Zhang (2015) as follows,

$$\begin{aligned} Y_{zc}(r, z) &= \left(\epsilon_{xc}(r_s(r, z)) \right. \\ &\quad \left. \frac{r_s(r, z) d\epsilon_{xc}(r_s(r, z))}{3 dr_s} \right) \frac{\hbar^2}{m_e a_0} \\ r_s(r, z) &= \frac{\sqrt[3]{3}}{a_0 \sqrt[3]{4\pi n_\rho(\vec{r})}} \\ \epsilon_{xc}(r_s(r, z)) &= \epsilon_x(r_s(r, z)) + \epsilon_c(r_s(r, z)) \\ \epsilon_x(r_s(r, z)) &= -\frac{3}{4} \sqrt[3]{\left(\frac{3}{2\pi}\right)^2 \left(\frac{1}{r_s(r, z)}\right)} \\ \epsilon_c(r_s(r, z)) &= -2A \left(1 + a_1 r_s(r, z)\right) \ln \left(1 + \frac{1}{2A\kappa(r, z)}\right) \\ \kappa(r, z) &= b_1 \sqrt{r_s(r, z)} + b_2 r_s(r, z) + b_3 \sqrt{r_s^3(r, z)} \\ &\quad + b_4 r_s^c(r, z) \end{aligned}$$

Where $r_s(r, z)$ is the local Seitz radius, $\epsilon_{xc}(r_s(r, z))$ is the combined exchange correlation energies, being $\epsilon_x(r_s(r, z))$ the exchange energy and $\epsilon_c(r_s(r, z))$ the correlation energy respectively. On the other hand, in the Kohn-Sham local density approximation Perdew and Wang (1992) the parameters

$\kappa(r, z)$, c , A , a_1 , b_1 , b_2 , b_3 , and b_4 are parametrized constants obtained using the random phase approximation Perdew and Wang (1992).

A.1. Eikonal equation:the reciprocal distance to walls

In COMSOL the Wall Distance interface calculates the reciprocal distance to selected walls. The value will be small when the object is far away from the respective walls and larger when closer. The exact distance, D , to the closest wall can be found by solving the Eikonal equation $|\nabla D| = 1$, where $D = 0$ on selected walls and $\nabla D \cdot \vec{n} = 0$ on other boundaries. COMSOL solves for a modified version of the Eikonal equation, where the dependent variable is changed from D to $G = 1/D$ and an additional smoothing parameter, σ_ω , is used. This results in the following equation:

$$\nabla G(\vec{r}) \cdot \nabla G(\vec{r}) + \sigma_\omega G(\vec{r}) (\nabla \cdot \nabla G(\vec{r})) = (1 + 2\sigma_\omega) G^4(\vec{r})$$

with $G(\vec{r}) = G_0 = 2/\ell_{ref}$ on selected walls and homogeneous Neumann conditions on the other boundaries. Here, ℓ_{ref} is a parameter that depends on the geometric shape and is calculated automatically. This parameter can also be defined manually, if necessary. The resulting wall distance, $D(\vec{r}) = 1/G(\vec{r}) - 1/G_0$, and the direction to the nearest wall are available in COMSOL as predefined variables.

B. Hamiltonian operator

The Hamiltonian operator of any media can be divided into two parts. On the one hand, there is the kinetic energy, which in this case is represented by two terms: the one corresponding to the kinetic energy of the nucleus

$$H_{NKE} = - \sum_{n=1}^{N_c} \frac{\hbar^2}{2M_n} \nabla_n^2 []$$

and the kinetic energy of the electrons $H_{EKE} = - \sum_{l=1}^{N_e} \frac{\hbar^2}{2m_e} \nabla_l^2 []$. The second part which

corresponds to the potential energy is more complex, since there is the interaction electron-nucleus, electro-electro and nucleus-nucleus. Thus the energy of attraction between the nucleus and electrons is given by the expression $H_{ENA} =$

$$-\frac{1}{4\pi\epsilon_0} \sum_{n=1}^{N_c} \sum_{l=1}^{N_e} \frac{z_l q_e}{R_{nl}} [],$$

the energy of repulsion between electrons by the expression $H_{EER} = \frac{1}{4\pi\epsilon_0} \sum_{l=1}^{N_e} \sum_{m \neq l}^{N_e} \frac{q_e^2}{r_{lm}} []$ and the

expression of repulsion between nuclei by the expression $H_{NNR} = \frac{1}{4\pi\epsilon_0} \sum_{n=1}^{N_c} \sum_{l \neq n}^{N_c} \frac{z_n z_l}{R_{nl}} []$. All these contributions configure the expression of the Hamiltonian operator.

$$H = H_{NKE} + H_{EKE} + H_{ENA} + H_{EER} + H_{NNR} \quad (28)$$

In the simplest cases, we can use these expressions since we know their variables, but in the most complex cases, such as the one we are dealing with, we have to model the effect of the Hamiltonian potential by means of an approximation. In the mean field theory $H_{ENA} + H_{EER} +$

$H_{NNR} \simeq \Phi(r, z)$. With this approximation we resort to two important simplifications. The first is that we neglect the kinetic energy of atomic nuclei and the second is that we assume an effective mass for the electrons (Hartree-Fock approximation Froese Fischer (1987)). This effective mass will be given by an effective mass tensor. The system of equations that we actually solve in matrix representation is given by the following expression:

$$\sum_{n=1}^N H_{mn} \psi_n^i(\vec{r}) = E^i \psi_m^i(\vec{r})$$

$$H_{mm} = \begin{cases} H_{mm} + V_{mm} \\ H_{mm} + \frac{\hbar^2}{2} \nabla \cdot (m_{eff,mm}(\vec{r})^{-1} \cdot \nabla) \end{cases}$$

$$V_{mm} = V_{mm} + V_{e,mm}$$

$$m_{eff,mm} = m_{eff,e,mm}$$

$$\psi_n^i(r, \theta, z) = \psi_n^i(r, z) e^{-jm\theta}$$

$$\Psi_m^i = \frac{\psi_m^i}{\sqrt{\sum_{n=1}^N \langle |\psi_n^i|^2 \rangle}}$$

References

- Agency, I.E., . Iea (2021), world energy outlook 2021, iea, paris <https://www.iea.org/reports/world-energy-outlook-2021>.
- Aldana, S., García-Fernández, P., Romero-Zalaz, R., Jiménez-Molinos, F., Gómez-Campos, F., Roldán, J.B., 2018. Analysis of conductive filament density in resistive random access memories: a 3d kinetic monte carlo approach. *Journal of Vacuum Science & Technology B* 36, 062201.
- Alicia Valero, A.V., 2014. Thanatia: the Destiny of the Earth's mineral resources. *A Thermodynamic Cradle to Cradle Assessment*.
- Altmann, S., 2013. *Band Theory of Metals: The Elements*. Elsevier Science.
- Ang, L.K., Kwan, T.J.T., Lau, Y.Y., 2003. New scaling of child-langmuir law in the quantum regime. *Phys. Rev. Lett.* 91, 208303.
- Balasubramanian, V., 2021. Brain power. *Proceedings of the National Academy of Sciences* 118, e2107022118.
- Banerjee, S., Zhang, P., 2019. A generalized self-consistent model for quantum tunneling current in dissimilar metal-insulator-metal junction. *AIP Advances* 9, 085302.
- Bates, D., 2013. *Quantum Theory: Elements*. Pure and applied physics, Elsevier Science.
- Biswas, D., Ramachandran, R., 2017. The image-charge correction for curved field emitters. *Physics of Plasmas* 24, 073107.
- BORDERA JUAN, T.A., 2022. EL OTOÑO DE LA CIVILIZACIÓN. CTXT.
- Callegari, A., Cartier, E., Gribelyuk, M., Okorn-Schmidt, H.F., Zabel, T., 2001. Physical and electrical characterization of hafnium oxide and hafnium silicate sputtered films. *Journal of Applied Physics* 90, 6466–6475.
- Ceballos, G., Ehrlich, P.R., Dirzo, R., 2017. Biological annihilation via the ongoing sixth mass extinction signaled by vertebrate population losses and declines. *Proceedings of the National Academy of Sciences* 114, E6089–E6096.
- COMSOL, . Comsol multiphysics software. <https://www.comsol.com/>.
- Cowie, R.H., Bouchet, P., Fontaine, B., 2022. The sixth mass extinction: fact, fiction or speculation? *Biological Reviews* 97, 640–663.
- D. Maldonado, C. Aguilera-Pedregosa, G.V.H.G.S.H.C.S.A.M.G.E.M.F.J.M.F.C.J.R., 2022. An experimental and simulation study of the role of thermal effects on variability in tin/ti/hfo2/w resistive switching nonlinear devices. *Chaos, Solitons and Fractals: the interdisciplinary journal of Nonlinear Science, and Nonequilibrium and Complex Phenomena*.
- Desai, P.D., Chu, T.K., James, H.M., Ho, C.Y., 1984. Electrical resistivity of selected elements. *Journal of Physical and Chemical Reference Data* 13, 1069–1096.
- Dyos, G., Farrell, T., 2012. *The Handbook of Electrical Resistivity* Edited by G. Dyos New materials and pressure effects. The Institution of Engineering and Technology.
- Frank, R.I., Simmons, J.G., 1967. Space-charge effects on emission-limited current flow in insulators. *Journal of Applied Physics* 38, 832–840.
- Froese Fischer, C., 1987. General hartree-fock program. *Computer Physics Communications* 43, 355–365.
- Funck, C., Menzel, S., 2021. Comprehensive model of electron conduction in oxide-based memristive devices. *ACS Appl. Electron. Mater.* 3, 3674–3692.
- Hui, F., Liu, P., Hodge, S.A., Carey, T., Wen, C., Torrisi, F., Galhena, D.T.L., Tomarchio, F., Lin, Y., Moreno, E., Roldan, J.B., Koren, E., Ferrari, A.C., Lanza, M., 2021. In situ observation of low-power nanosynaptic response in graphene oxide using conductive atomic force microscopy. *Small* 17, 2101100.
- I'chenko, L., Goraychuk, T., 2001. Role of the image forces potential in the formation of the potential barrier between closely spaced metals. *Surface Science* 478, 169–179.
- Lau, Y.Y., Chernin, D., Colombant, D.G., Ho, P.T., 1991. Quantum extension of child-langmuir law. *Phys. Rev. Lett.* 66, 1446–1449.
- Lin, J., Guha, S., Ramanathan, S., 2018. Vanadium dioxide circuits emulate neurological disorders. *Frontiers in Neuroscience* 12.
- Lin Wu, Huigao Duan, P.B.M.B.J.K.W.Y., Li, E., 2012. Fowler–nordheim tunneling induced charge transfer plasmons between nearly touching nanoparticles. *American Chemical Society*.
- MATLAB, . Matlab & simulink - mathworks. <https://la.mathworks.com/products/matlab.html>.
- Nations, U., 2022. The intergovernmental panel on climate change <https://www.ipcc.ch/>.
- Perdew, J.P., Wang, Y., 1992. Accurate and simple analytic representation of the electron-gas correlation energy. *Phys. Rev. B* 45, 13244–13249.
- Pérez, E., Maldonado, D., Acal, C., Ruiz-Castro, J., Alonso, F., Aguilera, A., Jiménez-Molinos, F., Wenger, C., Roldán, J., 2019. Analysis of the statistics of device-to-device and cycle-to-cycle variability in tin/ti:al:hfo2/tin rrams. *Microelectronic Engineering* 214, 104–109.
- Roldán, J.B., González-Cordero, G., Picos, R., Miranda, E., Palumbo, F., Jiménez-Molinos, F., Moreno, E., Maldonado, D., Baldomá, S.B., Moner Al Chawa, M., de Benito, C., Stavrinides, S.G., Suñé, J., Chua, L.O., 2021. On the thermal models for resistive random access memory circuit simulation. *Nanomaterials* 11.
- Rose, A., 1955. A space-charge-limited currents in solids. *Phys. Rev.* 97.
- Society, T.M.P., 2018. <https://www.mpg.de/12035093/brain>.
- Zhang, P., 2015. Scaling for quantum tunneling current in nano- and subnano-scale plasmonic junctions. *Sci Rep* 5.